# Optimizing Gold-Assisted Exfoliation of Layered Transition Metal Dichalcogenides with (3-Aminopropyl)triethoxysilane (APTES): A Promising Approach for Large-Area Monolayers

*Nicolò Petrini, Ermes Peci, Nicola Curreli,\* Emma Spotorno, Nastaran Kazemi Tofighi, Michele Magnozzi, Francesco Scotognella,\* Francesco Bisio,\* and Ilka Kriegel\**

Two-dimensional transition metal dichalcogenides (2D TMDCs) have gained significant attention from the scientific community due to their exceptional properties. Recently, the metal-assisted exfoliation technique has emerged as a promising method for producing large-area, high-quality 2D monolayers. However, achieving strong adhesion between metal foil and substrate during the exfoliation process remains a major challenge, preventing successful exfoliation. To overcome this issue, this study explores the application of (3-Aminopropyl)triethoxysilane (APTES) as an adhesion layer to substantially improve adhesion between the monolayers and hydrophilic substrates such as $SiO_2$, allowing for a high yield of mm-sized monolayers. Two sample sets, obtained from the same $MoS_2$ crystal via gold-assisted exfoliation with APTES-treated substrates and from standard scotch tape exfoliation, are statistically compared. APTES significantly improves exfoliation performance, yielding larger monolayers compared to conventional methods. This improvement enables the effective exfoliation with the gold-tape method, which otherwise results in no yield. Through Raman and photoluminescence characterization techniques, it is found that the flakes obtained from gold-assisted exfoliation and APTES are comparable to those obtained by standard scotch-tape exfoliation in terms of defects and optical properties, showing signatures of strain-induced Raman shift and n-type doping.

## 1. Introduction

Two-dimensional Transition Metal Dichalcogenides (2D TMDCs) with the formula $MX_2$ (M = Mo, W; X = S, Se) constitute a class of semiconductors known for their distinctive electrical and optical properties. These materials possess a direct bandgap, robust photoluminescence (PL), and significant exciton binding energy, making them promising candidates for a large plethora of opto-electronic devices.[1–3] Additionally, the van der Waals (vdW) gaps between each adjacent layer, coupled with their surface area, make them highly attractive for applications in capacitive energy storage, such as supercapacitors and batteries, as well as in sensing technologies.[2,4,5] Consequently, extensive exploration of these materials has allowed for the investigation of their fundamental properties and the unlocking of their potential for diverse technological applications.[6,7] In this context, a pivotal goal is the successful exfoliation of defectless single-crystal monolayers from their bulk counterparts.

N. Petrini, N. Curreli, N. Kazemi Tofighi, I. Kriegel
Functional Nanosystems
Italian Institute of Technology
via Morego 30, Genoa 16163, Italy
E-mail: nicola.curreli@iit.it; ilka.kriegel@iit.it
N. Petrini
Department of Physics
University of Genoa
via Dodecaneso 33, Genoa 16146, Italy

N. Petrini, N. Curreli
Molecular Foundry
Lawrence Berkeley National Laboratory
67 Cyclotron Rd, Berkeley, CA 94720, United States
E. Peci, E. Spotorno, M. Magnozzi
OptMatLab, Department of Physics
University of Genoa
via Dodecaneso 33, Genoa 16146, Italy
N. Curreli
Transport at Nanoscale Interfaces Laboratory
Empa
Swiss Federal Laboratories for Materials Science and Technology
Ueberlandstrasse 129, Dübendorf 8600, Switzerland
F. Scotognella
Department of Applied Science and Technology, DISAT
Polytechnic University of Turin
Corso Duca degli Abruzzi 24, Turin 10129, Italy
E-mail: francesco.scotognella@polito.it
F. Bisio
Institute of Superconductors
Innovative Materials, and Devices
CNR-SPIN, corso Perrone 24, Genoa 16152, Italy
E-mail: francesco.bisio@spin.cnr.it

**ADVANCED
SCIENCE NEWS**

www.advancedsciencenews.com

**ADVANCED
OPTICAL
MATERIALS**

www.advopticalmat.de

Several methods have been developed to achieve this, each presenting its unique set of advantages and challenges.[8–11] One widely employed top-down approach is scotch tape exfoliation, which relies on the weak vdW interactions between the layers in the bulk crystal.[6,8] However, this method suffers from limitations in terms of low yield, lack of uniformity in size and thickness, and challenges in scalability, making it less suitable for mass production.[12] On the other hand, chemical vapor deposition (CVD) is a bottom-up technique that employs molecular precursors to synthesize 2D material networks directly on substrates. CVD offers the advantage of producing large-area monolayers with controlled thickness and homogeneity. However, the process often introduces defects, grain boundaries, and impurities, potentially affecting the performance of the resulting 2D materials compared to exfoliated counterparts.[6,12] Moreover, fabrication of 2D materials via CVD requires precise control over precursors and deposition conditions for obtaining the desired outcome in terms of thickness, doping level, and crystalline orientation, depending also on the target substrate.[13,14] Additionally, the high furnace temperatures necessary for the CVD process can be incompatible with silicon-based technology processes.[15–17] This necessitates a transfer step from the CVD growth substrate to the intended target substrate.[18,19]

To address the limitations of conventional exfoliation methods, recent efforts have focused on the development of metal-assisted exfoliation techniques.[14,20] The metal-assisted exfoliation technique relies on the strong affinity between metals and the chalcogenide atoms in the TMDCs.[21–23] The process involves detaching TMDCs flakes from the bulk crystal owing to the binding force between the crystal and the metal surfaces, which surpasses the interlayer vdW forces. Consequently, this approach enables the production of large monolayer areas, offering scalability advantages over conventional scotch tape exfoliation method and the possibility to compete with CVD methods in terms of obtainable monolayer areas.[14,24] Among the various metals used for exfoliation, gold emerges as a prominent choice. However, multiple studies in literature have explored the use of additional metals alongside gold.[21,23,25,26]

The exploration of gold-assisted exfoliation presents promising opportunities, yet it faces many challenges in achieving an effective exfoliation process. The first issue revolves around the requirement for a clean, ultra-flat gold surface. Numerous approaches have been proposed to tackle this challenge. These range from from directly depositing the gold onto the bulk crystal,[27] to the exfoliation immediately after evaporation of gold film onto a supporting substrate,[24,28] to the cleaving of a thin gold layer that has been deposited on silicon ultra-flat wafer in combination with the support of thermal-release-tape (TRT).[20] This method ensures a consistently pristine surface in contact with the silicon wafer, allowing on-demand gold deposition onto the substrate while mitigating concerns related to aging and adsorbates. Another challenge lies in finding a viable technique to transfer the 2D flake from the gold layer to the target substrate. Some approaches employ a polymer-based wet transfer process, i.e. using PMMA or PDMS,[24] while others opt for a technique involving a TRT.[14,20] In the latter method, following annealing at the TRT release temperature, the TRT is expected to detach from the thin gold film, leaving the gold film and the exfoliated flake beneath it on the target substrate. However, despite its advantage

of avoiding direct polymer contact with the exfoliated flake, this approach presents an inherent challenge. The crucial issue is the complete and clean detachment of the TRT from the gold film during the thermal release process without causing damage to either the film or the exfoliated flake beneath. The TRT release procedure induces stress between gold and the substrate, potentially leading to gold and 2D material cracking or fragmentation if the adhesion between the gold foil and substrate is not sufficient. This poses a significant obstacle in achieving a flawless transfer of the exfoliated material onto the desired substrate. In our attempts to reproduce the gold-assisted exfoliation technique (e.g. from ref. [20]), as soon as the TRT reaches the release temperature point, the rapid thermal release process induces wrinkling and cracking on the gold surface. This disrupts the intended adhesion with the target substrate and undermines the integrity of the encapsulated exfoliated material. Consequently, this issue prevents the successful transfer of the exfoliated flakes onto the target substrate. Notably, this critical concern has largely been overlooked in most methodology descriptions in literature, posing a practical obstacle to achieving successful transfers and effective exfoliation. Moreover, the preparation of the target substrate is frequently underemphasized, if not entirely absent, in much of the available literature.[14,20,24,29] The adhesion properties of the target substrate are critical in both dry/wet transfer techniques and gold-assisted exfoliation processes. In the former, proper adhesion between the 2D material and the target substrate is necessary for effective transfer. For gold-assisted exfoliation, the significance of adhesion extends to both the bond between the substrate and the 2D material and importantly, between the substrate and the gold foil. Insufficient adhesion to the gold foil can lead to its damage during the TRT release phase, manifesting as cracks and wrinkles from the stress of TRT glue release. This damage adversely affects the 2D material beneath the gold foil, which, being strongly attached via vdW interactions to the gold layer, also cracks and detaches along with the gold layer. Consequently, ensuring robust adhesion between the gold carrier foil and the substrate is essential for successful exfoliation. Given the high sensitivity of 2D TMDCs to substrate characteristics such as surface roughness,[30] trapped charges,[31] adsorbates,[32] and hydrophobicity,[33] establishing a well-defined substrate preparation protocol in gold-assisted exfoliation becomes of paramount importance. For all these reasons, in this study, we investigate the use of (3-Aminopropyl)triethoxysilane (APTES) as an adhesion layer to foster strong binding between the gold thin film and the substrate.[34] By incorporating APTES into the process, we address the problem of the adhesion between the gold layer film carrying the exfoliated monolayer and the target substrate, thereby obtaining large 2D $MoS_2$ flakes with high yield. APTES also modifies the surface properties of the target substrate, increasing its affinity with gold,[35] preventing water penetration during the subsequent etching and cleaning processes. However, it is important to note that organic molecules like APTES can influence the optoelectronic properties of TMDCs, particularly $MoS_2$,[36–41] and thus, its effect needs to be investigated. Notably, we were unable to obtain useful results by using the gold-exfoliation technique without adding an APTES layer in the process. Hence, in this work, we comprehensively compared gold-exfoliated flakes with APTES substrate functionalization to those obtained through conventional scotch tape exfoliation. To assess process yield and

**ADVANCED
SCIENCE NEWS**

www.advancedsciencenews.com

**ADVANCED
OPTICAL
MATERIALS**

www.advopticalmat.de

monolayer quality we employed diverse techniques. First, optical microscopy images allowed for assessing the total yield of the process in terms of total exfoliated area and flakes dimension, confirming the superiority of APTES-based gold-exfoliation. Secondly, micro-ellipsometric images and atomic force microscopy (AFM) characterization were used to confirm the monolayer nature of the gold-exfoliated flakes. Note that micro-ellipsometry is more suitable for such large area flakes as it allows for investigation over a larger area (several millimeters), which is not possible with AFM (tens of micrometers). Subsequently, Raman and PL spectroscopy analysis indicated that the APTES layer likely influences both the stress and the doping of the exfoliated flakes, determining biaxial residual stress and n-type doping. Eventually, X-ray photoelectron spectroscopy confirms the presence of APTES which persists until the end of the exfoliation process. Our findings demonstrate the efficacy of APTES functionalization in the gold-assisted approach, which allows solving the adhesion issue between gold and the target substrate without compromising 2D TMDCs quality in terms of defects and optoelectronic properties, underlining its potential for producing large-area and high-quality monolayers.

## 2. Results and Discussion

We compared two sets of samples obtained from the same $MoS_2$ crystal. The first set comprised flakes obtained via gold-assisted exfoliation with substrates treated with a few nanometers thin layer of APTES. These substrates were subsequently used for the gold-assisted exfoliation process as reported by Liu et al. in ref. [20]. These samples are referred to as "$S_A$" samples, visually represented in green in the plots. As the benchmark for optoelectronic and crystalline quality and flake size, we chose traditional mechanical scotch tape exfoliation method on untreated $SiO_2$/Si substrates, since we were unable to perform a gold-assisted exfoliation without APTES functionalization in useful yield and size. Such samples are referred to as "$S_B$" samples, visually represented in blue in the plots. As mentioned earlier, the selection of APTES was motivated by the need for reliable adhesion in the release phase of the TRT adhesive. Without proper adhesion, the exfoliation process can be irreversibly compromised, leading to cracks in the gold layer that could damage the underlying 2D material and prevent its bonding with the substrate, hindering successful exfoliation. APTES was chosen from various self-assembled monolayers (SAMs) because it is effective in attaching gold to oxide substrates, as indicated in previous research.[34] This research[34] has shown that although thiol groups are recognized for their strong gold bonding capabilities due to sulfur atoms (Au-S bonding), APTES provides even stronger adhesion. Moreover, APTES was preferred over thiol-terminated compounds like (3-mercaptopropyl)methyltrimethoxysilane (MPTES) because its precursor is commonly used in atomic layer deposition (ALD) processes. This common use makes it readily available for controlled applications where precise adjustments of parameters and recipes are necessary for achieving consistent layer quality and even sample coverage. Further research on substrate functionalization with different SAMs[41] has demonstrated that APTES not only enhances the conductivity but also the optoelectronic properties of $MoS_2$ monolayers,[37,41] facilitating doping control of the 2D material. A graphical representation of the methodology used

is provided in Figure S1 (Supporting Information), where the modified exfoliation method utilizing APTES functionalization is illustrated in contrast with the conventional TRT gold exfoliation technique. Additionally, a more detailed description of the structure of APTES molecule and its grafting on the substrate is presented in the Supporting Information, with a corresponding visual representation featured in Figure S2.

### 2.1. Statistical Optical Characterization

**Figure 1** displays two examples of the exfoliation process using the gold-assisted technique with APTES and a standard scotch tape exfoliation, in order to visually highlight the differences between the two methods. In the case of the $S_A$ sample (Figure 1a), the gold-assisted exfoliation technique with APTES-functionalized substrates consistently yields large (> 1 mm$^2$), continuous monolayer flakes. Few flakes exhibit thickness larger than that of a monolayer, and in some cases, bulk structures are also present. Conversely, the $S_B$ samples (Figure 1b) exhibit a fragmented morphology characterized by small areas (∼ 2× $10^2$ µm$^2$) and a significant presence of few-layer and bulk structures (see the inset of Figure 1b for comparison, scale-bar 10µm). This aspect is particularly detrimental as it poses substantial challenges in identifying and isolating individual flakes suitable for device applications. Moreover, the close proximity of flakes to each other further complicates potential transfer processes, making it difficult to obtain well-defined isolated flakes. The lack of uniformity in thickness and the prevalence of fragmented structures in the $S_B$ samples limit their practical application.

These findings suggest that the gold-assisted exfoliation method with APTES treatment has the potential to produce a selective population of large-area flakes with monolayer thickness.

To quantitatively assess the yield of monolayer flakes from each method, we measured the size and area of these flakes across the entire chip. The Feret maximum diameter was employed for lateral size estimation.[42,43] Areas and Feret diameters were extracted using ImageJ particle analysis tool[44] by manually setting a suitable contrast threshold[45] (see Methods Section). In Figure 1c, we present the cumulative sum of flake area from several samples. This data is visualized using stacked bar plots, where each bar corresponds to a different sample, and each bin corresponds to a different flake. The flakes from the four analyzed scotch tape exfoliated samples were aggregated into a single representative $S_B$ sample. In the inset, we provide a magnified view of $S_B$ sample, since the y-scale, dictated by cumulative sum of gold-exfoliated samples, spans a too large range, making it impossible to identify details in sample $S_B$. This is primarily due to the fact that the total cumulative area of all the flakes in the scotch tape exfoliated samples does not exceed 500 µm$^2$. Conversely, in the case of the $S_A$ samples, we observe varying cumulative areas. Sample $S_{A_1}$ exhibited the smallest cumulative area, amounting to ∼ 15 mm$^2$, while $S_{A_6}$ demonstrated the largest cumulative area, amounting to ∼35 mm$^2$.

Next, we analyzed the lateral size distribution of the monolayer flakes in both $S_A$ and $S_B$ samples. By plotting count distribution functions, we visualized the spread of flake sizes for each method. Figures 1d and e depict respectively the area and size distributions organized in histograms for one representative
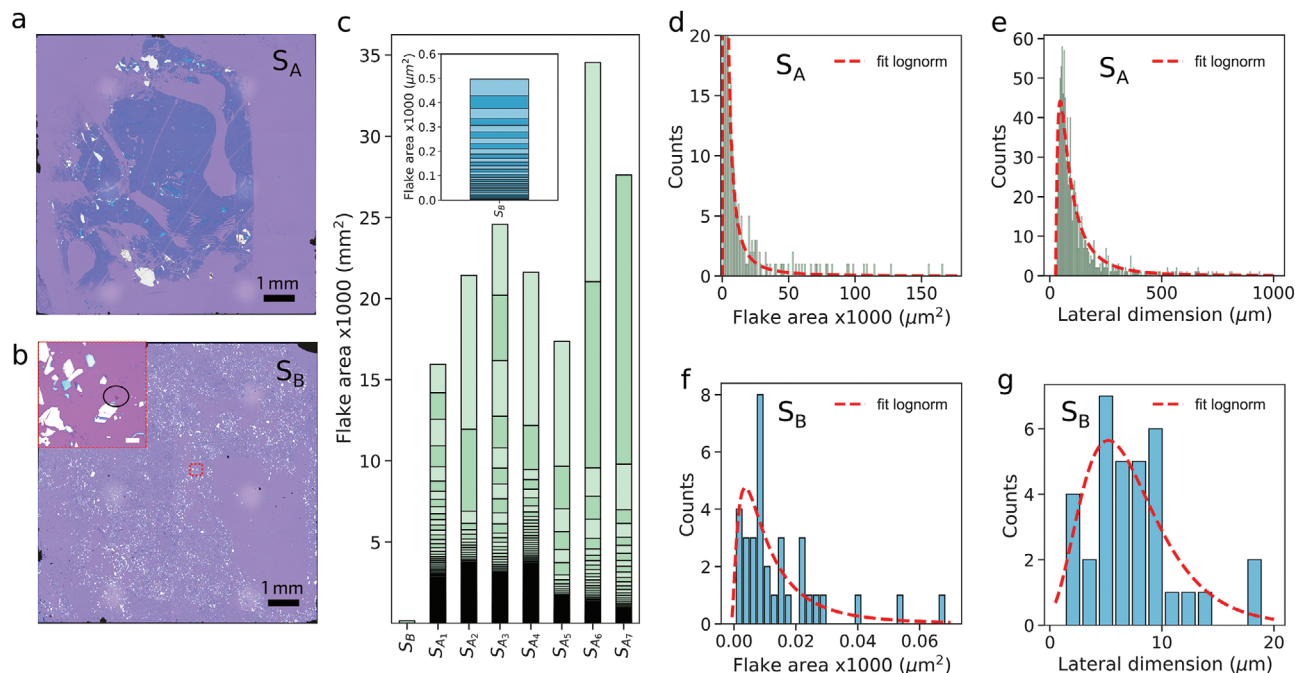
**Figure 1.** a) Optical image of flakes obtained via gold-assisted exfoliation with substrates treated with APTES ($S_A$). b) Optical image of flakes obtained via scotch tape exfoliation ($S_B$). Optical images were obtained by stitching 9 images obtained with 2.5× objective magnification. $MoS_2$ flakes can be distinguished thanks to a different optical contrast with respect to the substrate, ranging from dark violet (monolayer), to blue (multilayer), and white (bulk). The inset of panel b shows a magnification over an area where a monolayer flake is indicated by a black circle (inset scale bar 10 μm). c) Cumulative sum of the flakes area. Each column corresponds to a different sample, except column $S_B$, which aggregates all the monolayer flakes obtained via scotch tape exfoliation across four samples. Within each column, the stacked bins represent individual flakes, arranged in ascending order by size. To enhance clarity, two alternating shades of green are employed for $S_A$ samples and two shades of blue for $S_B$ samples. d) Distribution of flake area of the optical image of one $S_A$ sample depicted in panel a. e) Distribution of flake lateral size (Feret maximum diameter) of the optical image of one $S_A$ sample depicted in panel a. f) Distribution of flake area of the optical image of one $S_B$ sample depicted in panel b. g) Distribution of flake lateral size (Feret maximum diameter) of the optical image of one $S_B$ sample depicted in panel b. The four distributions are fitted with log-normal distribution, which can be visualized by the red dashed curves. Fitting parameters and statistical significance values can be found in Table 1.

$S_A$ sample, while Figure 1f and Figure 1g show the same quantities in histograms for representative $S_B$ sample. Mean, mode, median, and standard deviation (STD) were calculated to provide insights into the average flake size and the variability among flakes, as reported in **Table 1**. Statistical analysis was conducted on these distributions to compare the outcomes of the two exfoliation processes. Several statistical distributions were fitted and the goodness of fit was compared using the Kolmogorov-Smirnov statistical test (KS-test) and the p-value derived from it. A more detailed comparison of different statistical distributions is available in the Supplementary Information. The log-normal distribution was chosen for the statistical analysis of areal and lateral size distributions due to its relevance in the field of fragmentation

processes, especially within the realm of 2D fragmentation.[46–49] We evaluated the suitability of this distribution by computing the p-value using the KS-test. It was observed that, besides the significant lateral and areal size, the distribution fit of the data resulted in different KS-test p-values for $S_A$ and $S_B$ samples (Table 1).

Notably, the log-normal fit is suitable for $S_B$ samples (p-value > 0.05) but not $S_A$ samples (p-value < 0.05), indicating that the log-normal distribution might not be the appropriate choice for describing the fragmentation in the gold-assisted exfoliation. In particular, when comparing the survival function derived from different probability density function (PDF) fits (including log-normal, gamma, generalized-extreme-value distribution) of the experimental data, it is possible to assert that the log-normal

**Table 1.** Derived quantities and parameters of log-normal fit for $S_A$ and $S_B$ samples.

| | Mean (μm²) | Mode (μm²) | Variance (μm²) | STD (μm²) | p-value | RMSE | R-square |
|---|---|---|---|---|---|---|---|
| Area Flake $S_A$ | 8606.85 | 319.704 | 13803600 | 2303.81 | 0.01463 | 0.06784 | 0.29487 |
| Area Flake $S_B$ | 14.986 | 3.65333 | 0.32391 | 899.634 | 0.82744 | 1.13726 | 0.56631 |

| | Mean (μm) | Mode (μm) | Variance (μm) | STD (μm) | p-value | RMSE | R-square |
|---|---|---|---|---|---|---|---|
| Lateral dimension $S_A$ | 133.687 | 46.3137 | 23024.1 | 1.03785 | 0.010666 | 1.34258 | 0.953491 |
| Lateral dimension $S_B$ | 7.29768 | 5.21293 | 17.9408 | 0.37795 | 0.97952 | 1.4935 | 0.59239 |

**2303228 (4 of 13)**

**ADVANCED
SCIENCE NEWS**

www.advancedsciencenews.com

**ADVANCED
OPTICAL
MATERIALS**

www.advopticalmat.de

distribution well fits the smaller values (flake areas <80000 μm$^2$) but fails to account for the larger area and lateral sizes observed in the distribution of gold-assisted flakes (more details in Supporting Information). This discrepancy can be intuitively explained by considering that a log-normal distribution can describe the size distribution of particles obtained in a fragmentation process only if it follows a Kolmogorov cascade process,[48–50] where the likelihood of a particle undergoing subdivision into smaller parts of varying sizes during a specific time interval is independent on the initial particle size. This comparison suggests that the flakes obtained from gold-exfoliation could be divided into two groups, one represented by the smaller flakes, effectively modeled by Kolmogorov fragmentation process and well described by the log-normal distribution; the second represented by the bigger area flakes, which are outliers in the log-normal distribution and undergo a different process, not subject to the Kolmogorov fragmentation. Hence, from this experimental evidence of different fragmentation, it is possible to conclude that the gold-assisted exfoliation physical mechanism for larger flakes is different from the one that leads to small fragments in the traditional scotch tape exfoliation. It is important to note that the p-value and the statistics derived from the KS-test might be misleading because the parameters used for their calculation were derived from the distribution fitting rather than being imposed. This could potentially lead to a misinterpretation of the goodness of the fit. A robust assessment of goodness of fit involves calculating the Root Mean Square Error (RMSE) and the coefficient of determination (r-squared) for the area and lateral size distributions. While the lateral size distributions for both gold-assisted exfoliation and scotch tape show confidence values exceeding 50% of the observations, the area distribution for gold-assisted exfoliation flakes yields a low r-squared value. This confirms that the log-normal distribution inadequately describes the probability density for this dataset. Our findings consistently demonstrate that the use of the gold-assisted exfoliation method in conjunction with APTES treatment ($S_A$ samples) produces monolayer flakes that exhibit not only uniformity but also a large area. In contrast, the scotch tape exfoliation technique ($S_B$ samples) yields flakes characterized by fragmentation, smaller lateral dimensions, and a significant presence of few-layer and bulk structures. To quantitatively analyze these differences, we considered the maximum area $A_{max}^{(i)}$ of the flakes obtained for each exfoliated sample $i$. We introduced a figure of merit denoted as $min_i\left(A_{max}^{(i)}\right)$, representing the minimum area among these maximum values. Remarkably, upon analyzing the $S_A$ samples, we observed that $min_i\left(A_{max}^{(i)}\right) > 1.7 \times 10^6$ μm$^2$. In contrast, for the $S_B$ samples, $min_i\left(A_{max}^{(i)}\right) < 100$ μm$^2$. Overall, our data highlights the prevalence of smaller-sized samples according to a log-normal distribution. Nevertheless, the gold-assisted exfoliation technique emerges as a standout method due to its unique capacity to generate and unveil significantly larger-sized samples at notably higher frequency compared to the scotch tape technique.

## 2.2. Imaging Spectroscopic Ellipsometry

In order to evaluate the thickness of our MoS$_2$ crystals across large areas, we employed Imaging Spectroscopic Ellipsometry (iSE). It provides spatially averaged spectra of ellipsometric quantities Ψ and Δ over large areas (typically in the order of 100 μm$^2$). In particular, iSE yields spatial distributions of Ψ and Δ for each wavelength, enabling the resolution of micrometer-scale features while probing millimeter-sized areas within a single acquisition. The ellipsometric quantities Ψ and Δ describe the change in light polarization upon reflection from a sample. They are defined from the ratio of the complex Fresnel reflection coefficients for p- and s-polarizations, denoted as $r_p$ and $r_s$, respectively:

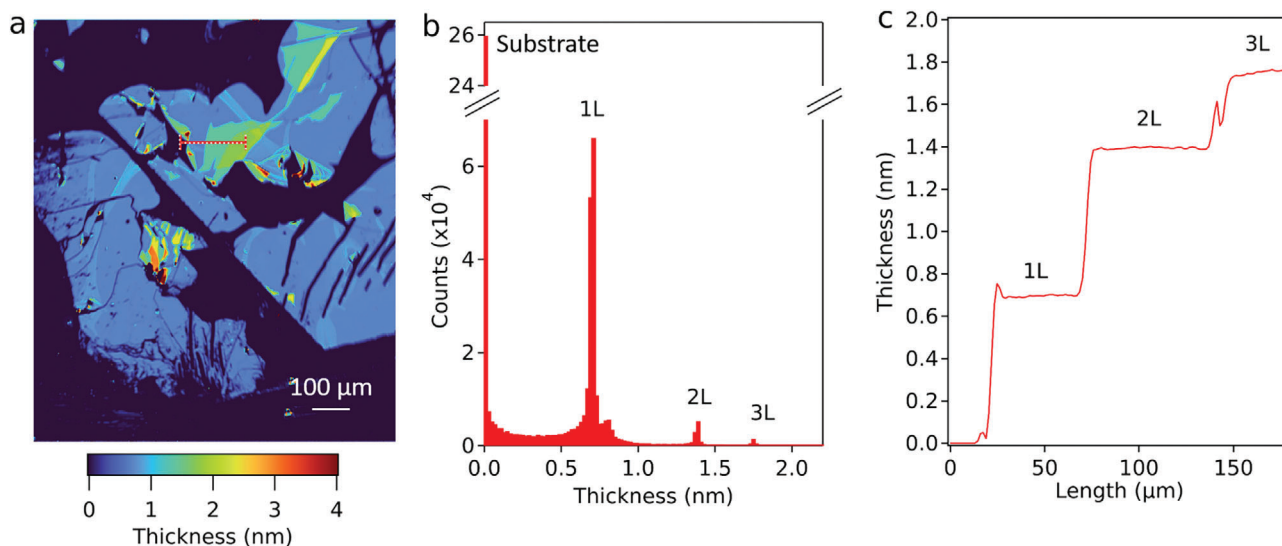$$\tan\Psi e^{i\Delta} = \frac{r_p}{r_s} \tag{1}$$

The Fresnel coefficients rely on both the dielectric function and the thickness of the sample materials, allowing these properties to be determined from Ψ and Δ spectra. Proper optical modeling enables the conversion of each Ψ and Δ spectrum into the local thickness value of a known thin film. The unique capabilities of iSE make it a valuable tool for investigating 2D TMDCs and their properties.[51,52]

Spatial maps of Ψ and Δ were acquired at six wavelengths within the relevant energy range, as described in the Experimental Section. The data was then converted into a thickness map using a layer-stack optical model comprising an optically semi-infinite Si substrate, a SiO$_2$ layer, and a MoS$_2$ layer. Optical constants for the MoS$_2$ layer were adopted from ref. [53], where the nominal thickness for 2D MoS$_2$ was set to 0.65 nm. The optical constants for Si and SiO$_2$ were provided by the instrument manufacturer. First, we determined the thickness of the SiO$_2$ layer by fitting its value on a clean area of the same MoS$_2$ monolayer. Subsequently, we performed pixel-by-pixel fitting of Ψ and Δ spectra to determine the local MoS$_2$ thickness, being the only free parameter in the optical model. Notably, the nanometer-thin APTES layer shares similar optical constants with the comparably thick (281 nm) SiO$_2$ layer beneath it,[54] and hence, for the purposes of this work, it is not treated as a separate entity. **Figure 2a** presents an illustrative thickness map of the MoS$_2$ layer of a $S_A$ sample, prominently displaying a large and uniform monolayer region with a thickness of 0.7 nm, along with distinctive features associated with multilayer areas. The thickness value of the monolayer is confirmed by AFM measurements, shown in Figure S3 (Supporting Information). Figure 2b shows the thickness distribution extracted from Figure 2a. Sharp peaks at 0.70, 1.38, and 1.75 nm correspond to monolayer, bilayer, and trilayer regions, respectively. Imaging spectroscopic ellipsometry thickness for bilayer and trilayer structures is lower than the expected one. This discrepancy arises because the optical constants of 2D TMDCs vary with the number of layers,[53] whereas our fitting is mainly targeted at identifying monolayer regions and, consequently, adopts the optical constants for monolayer MoS$_2$.

Figure 2c plots the line profile corresponding to the red line in Figure 2a. Sharp steps, associated with different numbers of layers, and consistent thickness values for each system highlight the versatility of iSE for thickness mapping over large areas of 2D materials.

## 2.3. Raman and Photoluminescence

To comprehensively investigate the diverse properties and physical phenomena within MoS$_2$ samples for both gold-exfoliation

**ADVANCED
SCIENCE NEWS**

www.advancedsciencenews.com

**ADVANCED
OPTICAL
MATERIALS**

www.advopticalmat.de

**Figure 2.** Layer thickness was assessed using Imaging Spectroscopic Ellipsometry (iSE) on a sample prepared via the gold-assisted technique with APTES. The thickness measurements were obtained from ellipsometric spectra through optical modeling and fitting. a) Mapping the thickness via iSE revealed a predominantly monolayer crystal of $MoS_2$. b) A histogram displaying thickness values from panel a. c) The thickness profile corresponding to the pink/red dashed line in panel a.

and scotch-tape exfoliation techniques denoted as $S_A$ and $S_B$ respectively, we conducted an in-depth analysis employing Raman and PL spectroscopy techniques.[55–61] In particular, Raman spectroscopy is highly effective in characterizing the thickness of exfoliated flakes by analyzing peak positions and evaluating the impact of substrates. This evaluation involves considering the structural modifications induced by strain and doping levels.[55,60,62] The samples treated with APTES revealed distinctive characteristics, notably exhibiting biaxial stress across the gold-exfoliated flakes and inducing an n-type doping effect.

In **Figure 3** illustrative Raman spectra from two samples $S_A$ (Figure 3a) and $S_B$ (Figure 3b), are depicted. Raman peaks were fitted to two Lorentzian components corresponding to the in-plane $E_{2g}^1$ mode (red dashed line) and the out-of-plane $A_{1g}$ mode (green-dashed line).[61,63] A shift in position of the in-plane $E_{2g}^1$ mode is usually associated to changes in strain within the material,[55,62] while position shift of $A_{1g}$ mode can instead be attributed to out-of plain stress induced by charged surface or doping changes.[14,55,64] In Figure 3c and Figure 3d we plot the position of each peak for both $S_A$ and $S_B$ samples, $Pos(E_{2g}^1)$ and $Pos(A_{1g})$, along with their relative shifts, $\Delta Pos(E_{2g}^1)$ and $\Delta Pos(A_{1g})$, respectively. Moreover, Figure 3e displays the intensity ratio between the out-of-plane and in-plane modes, denoted as $I(A_{1g})/I(E_{2g}^1)$, while Figure 3f showcases the full-width-half-maximum of $A_{1g}$, denoted as $FWHM(A_{1g})$. It is noteworthy that yellow data points in each plot represent monolayer flakes, whereas orange data points represent multilayers. To facilitate a clearer visualization of trends, boxplots were employed, accentuating the distribution spread along with the median value, emphasized by red lines within the box plots.

The Raman spectroscopy analysis depicted in Figure 3c reveals a distinct $\Delta Pos(E_{2g}^1) \sim 1.7$ cm$^{-1}$ shift between the gold-exfoliated samples ($S_A$) and the scotch-exfoliated ones ($S_B$). In particular, a $\sim 1.7$ cm$^{-1}$ redshift is observed from samples $S_A$ to $S_B$, which

can be attributed to either 0.80% of uniaxial strain or 0.36% biaxial strain in $S_B$ samples, according to [60]. Interestingly, despite the increased substrate roughness with APTES treatment, this condition does not determine a residual strain in $S_A$ samples. Instead, it is possible to hypothesize that the stress might be associated with flake dimensions, which are on average consistently larger for gold-assisted exfoliation as discussed in the previous paragraph. Therefore, residual strain can be correlated to border-induced effect,[65] which is more pronounced in the central area of scotch-exfoliated sample while relaxes within the larger flakes obtained by gold-assisted exfoliation. Kukucska et al. proposed a further method for verifying and quantifying the presence of strain by comparing $I(A_{1g})/I(E_{2g}^1)$ between samples $S_A$ and $S_B$.[55] For monolayer flakes, $I(A_{1g})/I(E_{2g}^1)$ increases by $\sim 28\%$ from samples $S_A$ to $S_B$ (Figure 3e). According to [55], this trend cannot be related to either uniaxial strain nor to biaxial strain in $S_B$ samples, because it is incompatible with the redshift observed from $S_A$ to $S_B$. Instead, only a $\sim -2\%$ of biaxial strain affecting $S_A$ samples could explain these combined trends. The analysis of $I(A_{1g})/I(E_{2g}^1)$ suggests the presence of strain, most probably associated with biaxial strain in APTES-treated samples. On the other hand, we found that $Pos(E_{2g}^1)$ demonstrates a negligible difference in multilayer samples, confirming that APTES primarily affects only the monolayer flakes. This observation aligns with the common understanding that the effects of strain tend to be more pronounced in very thin 2D material structures, with their influence diminishing as the number of layers increases.[55,62]
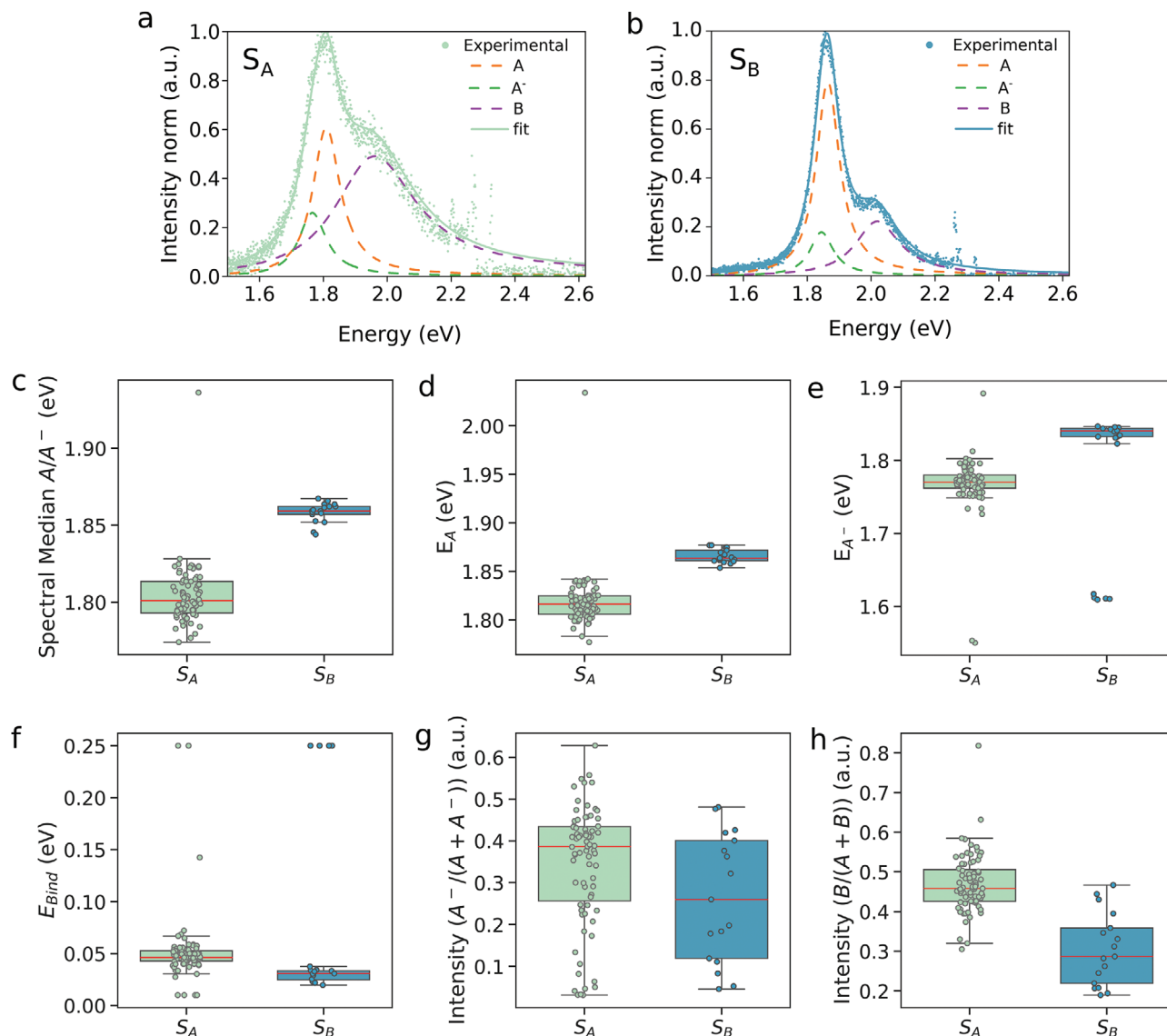
Furthermore, in considering the $A_{1g}$ peak, the observed softening in samples $S_A$ shown in Figure 3d may be attributed to several phenomena. Primarily, as this mode involves out-of-plane vibrations, alterations might arise from electronic interactions with the substrate, presenting a plausible explanation for this observed change. Hence, a different $Pos(A_{1g})$ can be lined to either out-of plain stress induced by a more electrically charged

2303228 (6 of 13)
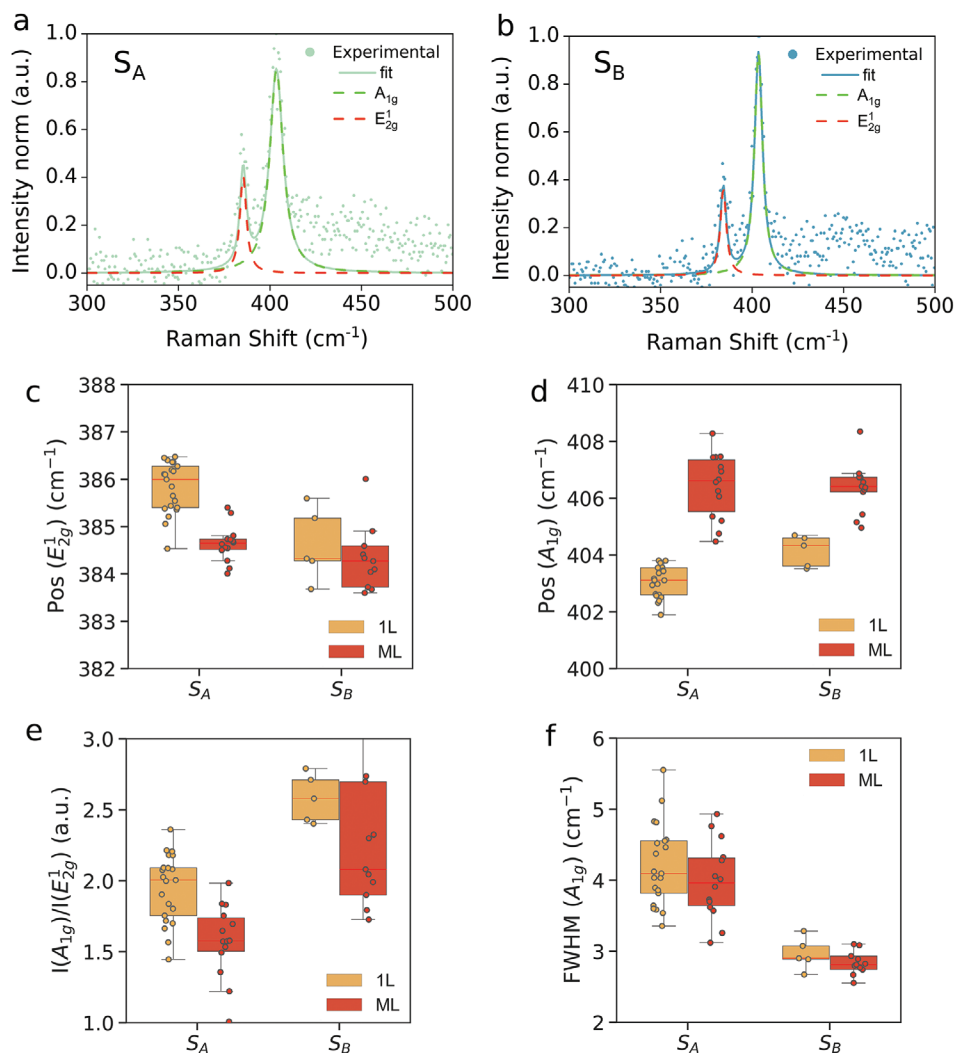
**Figure 3.** a) Typical Raman spectra of $S_A$ sample obtained from gold-assisted exfoliation. b) Typical Raman spectra of $S_B$ sample obtained from scotch tape exfoliation. The $E_{2g}^1$ and $A_{1g}$ modes are fitted with a double Lorentzian function, illustrating two contributions via the red dashed curve ($E_{2g}^1$) and green dashed curve ($A_{1g}$). c) Raman peak positions of the $E_{2g}^1$ mode over multiple spectra acquisition. d) Raman peak positions of the $A_{1g}$ mode over multiple spectra acquisition. e) $I(A_{1g})/I(E_{2g}^1)$ intensity ratio. f) Full-width at half maximum (FWHM) of $A_{1g}$ peak. The data points are organized in 4 boxplot graphs, divided between $S_A$ and $S_B$ samples on x-axis and grouped between monolayer flakes (yellow, 1L) and multilayer (orange, ML).

surface[14] or with a change of doping level in the $MoS_2$.[64] In the first hypothesis, the influence of APTES on the vibrational mode of $MoS_2$ could manifest due to the establishment of a distinct dielectric environment, different from the inherent properties of bare $SiO_2$. Notably, the positively charged functional amine group (-$NH_2$) in APTES might interact differently with sulfur (S) atoms compared to molybdenum (Mo) atoms. Such interactions could induce stiffening caused by the different interactions within a different charged landscape. Remarkably, this perturbation might solely affect the $A_{1g}$ mode without concurrent effects on the doping level of $MoS_2$, thus preserving the PL spectral shift and intensity.[14] Alternatively, the second hypothesis suggests that the APTES layer acts as an interface that can induce n-type electrical doping in $MoS_2$. This case is supported by previous studies of Kang et al., demonstrating that the amine group provides a positive pole charge, inducing a negative dipole moment on the $MoS_2$, making APTES act as n-type dopant.[37,41,66] Another indication of a change in doping level is suggested by the modulation of FWHM($A_{1g}$) as shown in Figure 3f, which increases in gold-exfoliated samples and which can be correlated with a higher doping level.[64] Furthermore, doping could potentially account for the disparities in both the intensity ratio $I(A_{1g})/I(E_{2g}^1)$ and the FWHM($A_{1g}$) observed among multilayer samples of $S_A$ and $S_B$ (Figure 3e and f, respectively). However, it is noteworthy that the Pos($A_{1g}$) does not consistently vary between the $S_A$ and $S_B$ samples, aligning with previous findings on doping in multilayer $MoS_2$.[67] If electrostatic doping and residual stress are attributable to the electrostatic interaction between APTES amine functional group and the $MoS_2$, feasible methods to modulate such dielectric environment are either changing the functional group exposed to the 2D material, as reported in the study by Najmaei et al.[41] or controlling the areal density of molecules

ADVANCED
SCIENCE NEWS

www.advancedsciencenews.com

ADVANCED
OPTICAL
MATERIALS

www.advopticalmat.de

**Figure 4.** Photoluminescence Analysis of $S_A$ and $S_B$ samples. a) Illustrative examples of typical PL spectra obtained from gold-assisted exfoliation with APTES ($S_A$ sample). b) Illustrative examples of typical PL spectra obtained from scotch tape exfoliation ($S_B$ sample). Excitons A, B and trion $A^-$ are fitted with a triple Lorentzian function: the three contributions can be visualized by the orange dashed curve (Exciton A), green dashed curve (trion $A^-$) and violet dashed curve (Exciton B). c) Spectral median, accounting only for exciton A and trion $A^-$, which is used to qualitatively assess the spectrum shift. Boxplot graphs are used to highlight the median of the measurements and the dispersion. Green color corresponds to gold-exfoliated samples $S_A$, blue color corresponds to scotch tape exfoliated samples $S_B$. d) Excitons A peak energy and e) trion $A^-$ peak energy. f) Binding energy of the trion. g) Intensity ratio between A and $A^-$, suggesting n-type doping in $S_A$. h) Intensity ratio between B exciton and A exciton, associated with the presence of defects that hinder non-radiative recombination processes.

forming the SAM. To verify the doping hypothesis more robustly, we employed PL spectroscopy, specifically focusing on the study of the ratio between charged excitons, $A^-$ known also as trions, and neutral excitons, A and B. For this reason, we have analyzed the PL of samples $S_A$ and $S_B$. Illustrative examples of PL spectra for $S_A$ and $S_B$ are shown in **Figure 4a** and b, respectively. Each spectrum was analyzed by fitting it with a triple Lorentzian model to account for excitons, A and B, and for the trion, $A^-$. First, in order to analyze the spectra, we considered the spectral median (Figure 4c), that is a derived quantity defined as the wavelength median value of the intensity spectrum. The spectral median con-

siders not only the peak position but also the intensity weight of each component of the spectrum. Since we are interested in particular into the excitons A and trion $A^-$, we only considered the spectral median relative to these two contributions, avoiding the B exciton contribution. We observe an overall shift towards higher energies in the spectral median for scotch tape exfoliated samples, depicting a notable blueshift of ∼58 meV. This blueshift can be caused by different factors, including a displacement in the wavelength position of the exciton/trion peak, a relative shift attributed to distinct binding energies, or variations in the intensity weight of these contributions.[57,68] The absolute spectral

**ADVANCED
SCIENCE NEWS**

www.advancedsciencenews.com

**ADVANCED
OPTICAL
MATERIALS**

www.advopticalmat.de

positions of exciton A and trion A⁻ are presented in Figure 4d and Figure 4e, respectively. Notably, both the exciton and the trion, exhibit a blueshift in peak position from gold-assisted exfoliated sample S_A to scotch tape exfoliated S_B. In particular, the shift for exciton A amounts to ∼ 47 meV, whereas for trion A⁻ is ∼ 62 meV. Consequently, the binding energy between exciton A and trion A⁻, defined as $E_{Bind} = E_A - E_{A^-}$, is higher in the case of gold-exfoliated samples by ∼15 meV (Figure 4f).[57,68,69] This increase in binding energy can be associated with electrostatic and/or chemical doping effects, as reported in ref. [68]. Nevertheless, the shift of the spectral median is not only associated with the individual peak shift of the excitonic contribution, but takes also into account the intensity of each contribution.[57,68]

Indeed, the spectral weight ratio between the trion and exciton intensities, depicted in Figure 4g, illustrates that the relative weight intensity of the charged exciton A⁻ is higher in the case of S_A than in S_B. It is well established that the intensity ratio $I_{A^-}/I_A$ can be correlated to the free electron $n_e$ concentration by considering the combination of the mass action model and a three-level emission model for the excitons A and trions A⁻,[59,60,68] resulting in the Equation 2:

$$n_e = \frac{I_{A^-}}{I_A} \cdot \frac{\tau_{A^-}}{\tau_A} \cdot \frac{4m^*}{\pi\hbar^2} \cdot k_B T \cdot e^{-\frac{E_{Bind}}{k_B T}} \qquad (2)$$

where $\frac{I_{A^-}}{I_A}$ is the trion/exciton intensity ratio, $\frac{\tau_{A^-}}{\tau_A} = 1/6.6$[59] is the ratio between the decay rates of trion/exciton, $m^* = \frac{m_A \cdot m_e}{m_{A^-}} = \frac{0.8 \cdot m_0 \cdot 0.35 \cdot m_0}{1.15 \cdot m_0}$, with $m_0$ being the free electron mass, $\hbar$ is the reduced Planck's constant, $k_B$ is the Boltzmann constant, $T$ is the temperature and $E_{Bind}$ is the trion binding energy. Since all the parameters are known from theory or can be experimentally determined ($E_{Bind}, I_{A^-}/I_A$), we can estimate that the electron density of S_A is approximately $5.5 \times 10^{12}$ cm⁻², while in S_B, it is $4.2 \times 10^{12}$ cm⁻². This demonstrates that in gold-exfoliated samples there is an additional source n-type doping that influences both PL and Raman data which can be ascribed to the presence of APTES.
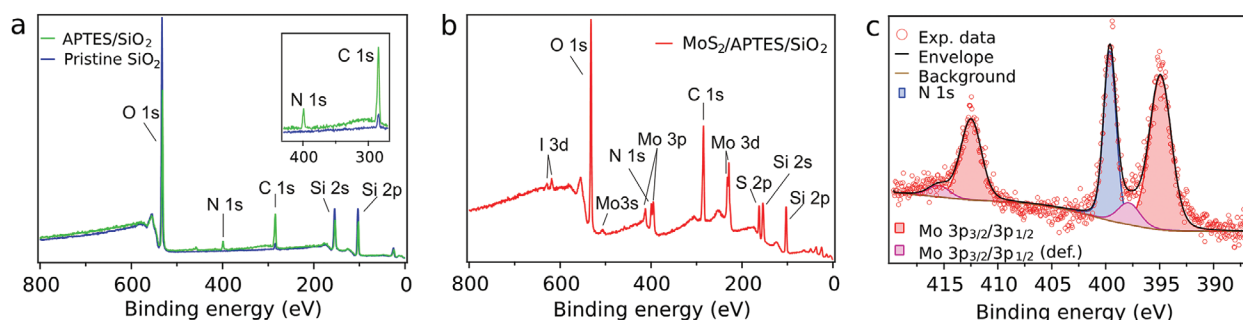
According to McCreaery et al.,[70] the relative intensities of A and B excitons serve as an indicator of non-radiative recombination and sample quality. A longer A⁻ exciton lifetime, indicative of low non-radiative defects, results in dominant A-exciton emission relative to B-exciton emission. Conversely, a high density of defects reduces the A-exciton lifetime, making the B-to-A relaxation pathway more probable, increasing B-exciton emission. Ji[40] and Najmaei's[41] findings suggest that modifications in substrate functionalization, such as intense oxygen plasma treatment inducing p-doping, can significantly alter the A-B intensity ratio.[40,41] Additionally, electrostatic doping through applied gate voltage, as reported by Liu et al.,[71] can also modify the A-B ratio. Combining these results, we can interpret our own results and assess sample defectivity more accurately.[40,41,70,71]

The observed differences in B-A exciton intensity ratio between samples S_A and S_B are depicted in Figure 4h, showing variations not exceeding an order of magnitude. It cannot be excluded completely that the several cleaning steps involved in the gold-exfoliation process do not contribute to an increase of defects, leading to the observed increase in B-A exciton from sam-

ples S_B to samples S_A. However, in both S_A and S_B samples, the high values of $I_B/(I_A + I_B)$ compared to literature values for MoS_2 suggest either a high defect density inherent to the bulk crystal or an effect induced by electrostatic p-doping from the SiO_2/Si substrate, influenced by its further functionalization in the case of APTES.[40,70,71] Given the consistently high B-A exciton ratio across different bulk crystals and exfoliation techniques, we are inclined to attribute this to substrate doping, indicating comparable defect densities for the two exfoliation methods. The differences B-A exciton ratio, not exceeding an order of magnitude, are likely due to variations in substrate functionalization and not to defectivity. Specifically, APTES functionalization, attributed to n-type doping from APTES amine presence, leads to an increase in the B-A intensity ratio. Furthermore, the comparable full width at half maximum (FWHM) of $E_{2g}^1$ Raman peak, reported for both samples in Figure S3 (Supporting Information), suggests comparable defectivity aligning with McCreaery et al., observations.[70] These observations indicate thus a comparable quality in terms of defectivity for both S_A and S_B samples, suggesting that the exfoliation method does not impact consistently on the quality, while APTES presence modifies doping level, affecting the optical response.

## 2.4. X-Ray Photoelectron Spectroscopy

X-ray photoelectron spectroscopy measurements were performed in order to assess the presence of the APTES molecule, both before and after the exfoliation process, and show that the APTES layer persists throughout the entire process. **Figure 5a** compares XPS survey spectra of a pristine SiO_2(285 nm)/Si substrate before and after APTES deposition. The presence of APTES on the surface is confirmed by the presence of the N 1s peak at 400 eV binding energy (BE) originating from the amine group (-NH_2). Similarly, the increase of the C 1s peak at 285 eV BE with respect to the clean substrate is due to the organic chain of APTES. Figure 5b shows the XPS survey spectra of a monolayer MoS_2 flake after the exfoliation process. Molybdenum and sulphur peaks are present, as expected, as well as the N 1s peak, confirming that APTES persists after the chemical processes involved in our exfoliation technique. The I 3d doublet at 618 eV/629 eV BE can be traced back to residues of the Au etchant (KI/I_2). No trace of potassium is observed; hence, only iodine is bound to the sample. A further analysis of the same region has been performed by acquiring and fitting XPS spectra with high spectral resolution; in particular, we investigated the Mo 3p/N 1s peaks (shown in Figure 5c), as well as the Mo 3d/S 2s, S 2p, and C 1s peaks (shown in Figure S2a–S2c, respectively). Figure 5c shows a high-resolution XPS spectrum of the N 1s peak and the Mo 3p doublet, together with their fitting curves. The main Mo $3p_{3/2}/3p_{1/2}$ peaks are located at 394.9 and 412.5 eV BE, respectively. A second Mo 3p doublet is present, with peaks at 397.9 and 415.4 eV BE; these states can be attributed to MoO_3 traces.[72] Similarly, higher BE states are observed in the Mo 3d doublets (Figure S3, Supporting Information). The N 1s peak (Figure 5c) is located at 399.6 eV BE and is attributed to the -NH_2 group of the APTES molecules.[73,74] The persistence of the N 1s peak throughout the exfoliation process and the absence of additional N 1s subcomponents afterward suggests that the APTES molecules

**ADVANCED
SCIENCE NEWS**

www.advancedsciencenews.com

**ADVANCED
OPTICAL
MATERIALS**

www.advopticalmat.de

**Figure 5.** XPS spectra depicting APTES and monolayer MoS$_2$ over APTES. a) XPS spectra of a pristine SiO$_2$ (285 nm)/Si substrate before and after APTES deposition. The N 1s peak acts as a fingerprint for the APTES molecule. The inset provides a detailed view of the N 1s and C 1s peaks. b) XPS spectrum of a monolayer MoS$_2$ crystal, confirming the persistence of the APTES layer during the exfoliation process. c) High-resolution XPS data and fitting of the Mo 3p and N 1s peaks of a monolayer MoS$_2$ crystal.

persist on the substrate and do not react during the exfoliation process.

## 3. Conclusion

In summary, we have presented a fully reproducible method for functionalizing the target substrate using APTES, thereby enabling high-yield gold-assisted exfoliation, otherwise not possible due to gold detachment in the release step of TRT. The comparison between samples obtained via gold-assisted exfoliation with APTES-treated substrates and standard scotch tape exfoliation revealed that APTES significantly enhances exfoliation performance compared to conventional methods. Gold-assisted exfoliation technique with APTES has demonstrated the production of significantly larger exfoliated areas, exceeding 1 mm$^2$ for all samples, in contrast to a maximum area of 80 μm$^2$ achieved with scotch tape exfoliation. Our study employed optical imaging to analyze the fragmentation process using statistical methods. We found that the gold exfoliation technique, when combined with APTES, generates small fragments that conform to a log-normal distribution, similar to the scotch tape method. However, unlike the latter, this technique also produces larger flakes. These outliers in the distribution suggest an alternative process less influenced by fragmentation. This process appears to facilitate the creation and preservation of large monolayer flakes. Despite the increased area, the overall properties exhibited changes in comparison to those obtained through scotch tape exfoliation. These changes manifest as residual biaxial strain effects, indicated by shifts in the $A_{1g}$ peak position, as well as n-type doping effects, characterized by a blueshift in the spectral median in the photoluminescence spectra and alterations in the exciton-trion ratio. The root cause of these changes can be attributed to the presence of APTES, which persists throughout the entire process, as confirmed by XPS measurements. Therefore, in addition to achieving larger flakes, we have also demonstrated that chemical doping through the APTES layer can be accomplished.

## 4. Experimental Section

*Scotch Tape Exfoliation*:    The target MoS$_2$ crystal was placed on scotch tape and folded multiple (5–10) times until obtaining thin and almost transparent flakes on the mother tape. The folding was stopped as soon as the flakes where optically thinned enough in order to avoid further fragmentation and lead to a larger lateral size. Then, target substrates of SiO$_2$/Si (285 nm/500 μm) previously treated with oxygen plasma were placed beneath the tape regions with a higher density of thin flakes, and then the tape was gently pressed onto the substrates. The ensemble was then heated on a hotplate at 100 °C for 5 min to promote adhesion and obtain larger flakes.[75] Eventually, the ensemble was let to cool down to room temperature and the scotch tape was removed, leaving the MoS$_2$ flakes on the SiO$_2$/Si substrate.

*Gold-Assisted Mechanical Exfoliation*:    The MoS$_2$ bulk crystal was purchased from HQ Graphene, Netherlands, with lateral crystal size of up to 8 mm. gold-assisted mechanical exfoliation was carried out using the approach detailed in ref. [20]. First of all, a 150 nm thick layer of Au was deposited onto a 285 nm SiO$_2$ (thermal oxide) / 500μm substrate wafer (SiMat, p-doped type) using sputter coater (KS500 Confocal, Kenosistec). The poor adhesion between gold and SiO$_2$ allowed the subsequent easy peel-off of gold from the SiO$_2$ surface. A solution of polyvinylpyrrolidone (Sigma–Aldrich, $M_w$ 55000, 10% wt dispersed in solution 1:1 wt of ethanol/acetonitrile) was then spin-coated onto the gold film and cured at 150 °C for 5 min, serving as a sacrificial layer to prevent contamination from tape residue. Thermal release tape (TRT) (Nitto Denko Revalpha RA95LS(N), with a 105 °C release temperature) is used to peel off the PVP/Au layer from the SiO$_2$/Si wafer, obtaining a metal-tape portion slightly bigger than the target substrate (10 mm lateral size) and the crystal surface. The TRT/PVP/Au ensemble was then pressed onto a freshly cleaved and ultra-flat surface of the MoS$_2$ bulk crystal, resulting in the exfoliation of the TMDC flakes, which remained adhered to the gold layer. Optical inspection of the gold surface reveals monolayer/multilayer as darker regions. The TRT was designed to be removed at a temperature of 105 °C, facilitating the transfer of the monolayer 2D crystal attached to the gold surface onto a Si/SiO$_2$ substrate. The exfoliated MoS$_2$ was then carefully transferred to the target substrate covered with APTES. To detach the TRT and ensure successful transfer, the TRT/PVP/Au/MoS$_2$ flake structure was placed on a hotplate preheated to 125 °C. Without any adhesion layer, the polymerization of the TRT glue at temperatures above the transition temperature would lead to cracks throughout the gold layer, and consequently the exfoliated TMDC flakes would not adhere to the target substrate. Thus, the use of an adhesion layer is crucial for the correct transfer of the MoS$_2$/Au/PVP structure to the target substrate. After successful transfer, the structure underwent a washing process to remove the protective PVP layer, the Au layer, and any other potential residues, leaving only the exfoliated TMDC on the substrate. The cleaning process involved the following steps: deionized (DI) water at 90 °C for 10 min, followed by acetone rinse at 70 °C for 10 min and rinse with isopropanol. The gold layer was dissolved using a KI/I$_2$ (Sigma–Aldrich) gold etchant solution for 3 min, and eventually the structure was thoroughly rinsed with MilliQ water, followed by a rinse with isopropanol to ensure cleanliness. If any organic process residues persisted after the washing process, the application of Microposit MF 319 in conjunction with N-Methyl-2-pyrrolidone (NMP) was found effective in eliminating them.[76]

*Atomic Layer Deposition of APTES*: Si/SiO$_2$ substrates were functionalized by means of atomic layer deposition (ALD). After oxygen plasma cleaning, Si/SiO$_2$ substrates were placed inside the ALD chamber (Oxford Atomic layer deposition system), which was purged with nitrogen gas. Subsequently, the APTES precursor was introduced into the ALD chamber, and the deposition was carried out at 110 °C. The APTES precursor was pulsed into the chamber, allowing it to react with the substrate surface, employing 30 pulses cycles of APTES deposition. The use of more pulsed cycles ensured the deposition of a uniform monolayer of APTES over the entire surface, while the total thickness of the layer remained unaffected by the number of cycles.[77]

*Monolayer Identification with Optical Contrast*: The method of optical contrast for identifying monolayers of 2D materials over a specific substrate is widely acknowledged.[45,78–80] The optical images acquired with Zeta 20 Optical Profilometer were then processed with ImageJ software[44] for analyzing the optical contrast regions corresponding to the monolayer optical contrast.[45] The optical images were splitted in the RGB channels and red channel was analyzed, since the best contrast was provided by this channel. ImageJ threshold routines for particle identification and analyses were employed for calculating the monolayer areas and the lateral size (Feret maximum diameter), then statistical fitting employing log-normal distribution was applied for the analysis of the distributions.[46,47] It is important to note that when analyzing the entire surface of the substrate in gold-exfoliated samples, we used a 2.5× magnification with a minimum pixel size corresponding to 3.5 µm. In contrast, for scotch tape exfoliation, where the flakes were considerably smaller, optical inspection was performed across the entire sample, and any found flakes were subsequently analyzed at higher magnification, yielding a more precise minimum size (0.366 µm per pixel, 20× objective). This difference in magnification affects the minimum detectable fragment size when using ImageJ but preserves the ability to identify large areas. This distinction is crucial for analyzing gold-assisted exfoliation images, as our primary focus is on these larger areas.

*Imaging Spectroscopic Ellipsometry*: iSE maps were acquired using an Accurion nanofilm_ep4 imaging ellipsometer equipped with a LedHUB® light source. The angle of incidence (AOI) was kept at the relatively small value of 50° in order to maximize the signal-to-noise ratio. iSE measurements were performed with a 5 × objective and the imaging ellipsometer operated in nulling mode. In this mode, the nulling ellipsometry principle is applied to each pixel of a CCD camera placed at the end of the analyzer arm, hence allowing to measure at once the whole area of interest. A further improvement in the quality of the Ψ and Δ maps is achieved by automatically scanning over the focal position of the objective, as only one line at a time is perfectly focused due to the oblique orientation of the arm. The wavelengths provided by the light source are 386.7, 443.8, 522.5, 595.0, 659.6 and 844.6 nm. A map of Ψ and Δ was acquired at each wavelength and all of them were used for the subsequent thickness fitting process.

*Micro-Photoluminescence and Micro-Raman*: A CW laser (Edinburgh Instruments) at 532 nm was used for excitation of the MoS$_2$ flakes. The laser light was coupled into IX83 Olympus inverted microscope and focused on the samples by means of ×60 (N.A. 0.8) Olympus microscope objective lens. The spot position was adjusted with the movement of the sample stage, controlled by means of Physik Instrumente (PI) double M-229 Linear Actuators, coupled with PI M-405 Precision Translation Stage and operated with PIMikroMove software and C-819 joystick (PI). The emitted photoluminescence signal was collected by the same objective and sent to HRS-500 spectrometer (Princeton Instruments) for dispersion. The grating used for dispersion had 500 nm blaze wavelength, 150 grooves/mm with 650 nm center wavelength. The dispersed signal was then detected through PIXIS CCD camera (Princeton Instruments) and acquired employing LightField (Princeton Instruments) software.

Raman measurements were conducted with the same setup, except for using a different spectrometer dispersion grating (500 nm blaze wavelength, 1800 grooves/mm, 542 nm center wavelength).

For all measurements, the excitation power was 50 µW in order to keep the photoluminescent response in the linear regime.

*X-Ray Photoelectron Spectroscopy*: XPS was performed using a Physical Electronics PHI 5800 spectrometer equipped with a monochromatized Al K$_\alpha$ source. The X-ray spot size was few-hundred microns, allowing to probe a uniform large-area monolayer of MoS$_2$. Charge correction was made by setting the lowest energy component of the C 1s peak at 284.5 eV. XPS data analysis and fitting were performed with the commercial software CasaXPS version 2.3.25.

## Supporting Information

Supporting Information is available from the Wiley Online Library or from the author.

## Conflict of Interest

The authors declare no conflict of interest.

## Data Availability Statement

The data that support the findings of this study are available from the corresponding author upon reasonable request.

[1] Q. H. Wang, K. Kalantar-Zadeh, A. Kis, J. N. Coleman, M. S. Strano, *Nat. Nanotechnol.* **2012**, *7*, 699.

[2] F. Bonaccorso, L. Colombo, G. Yu, M. Stoller, V. Tozzini, A. C. Ferrari, R. S. Ruoff, V. Pellegrini, *Science* **2015**, *347*, 1246501.

[3] A. Asaithambi, N. Kazemi Tofighi, N. Curreli, M. De Franco, A. Patra, N. Petrini, D. Baranov, L. Manna, F. D. Stasio, I. Kriegel, *Adv. Opt. Mater.* **2022**, *10*, 2200638.

[4] O. Lopez-Sanchez, D. Lembke, M. Kayci, A. Radenovic, A. Kis, *Nat. Nanotechnol.* **2013**, *8*, 497.

[5] M. Ghini, N. Curreli, A. Camellini, M. Wang, A. Asaithambi, I. Kriegel, *Nanoscale* **2021**, *13*, 8773.

**ADVANCED
SCIENCE NEWS**

www.advancedsciencenews.com

**ADVANCED
OPTICAL
MATERIALS**

www.advopticalmat.de

[6] A. Asaithambi, N. Kazemi Tofighi, M. Ghini, N. Curreli, P. J. Schuck, I. Kriegel, *Chem. Commun.* **2023**, *59*, 7717.

[7] S. S. Sunku, D. Halbertal, R. Engelke, H. Yoo, N. R. Finney, N. Curreli, G. Ni, C. Tan, A. S. McLeod, C. F. B. Lo, C. R. Dean, J. C. Hone, P. Kim, D. N. Basov, *Nano Lett.* **2021**, *21*, 1688.

[8] F. Bonaccorso, A. Lombardo, T. Hasan, Z. Sun, L. Colombo, A. C. Ferrari, *Mater. Today* **2012**, *15*, 564.

[9] X. Huang, X. Han, Y. Dai, X. Xu, Y. Zhang, X. Tian, Z. Yuan, J. Xing, Y. Wang, Y. Huang, *J. Phys. Chem. Lett.* **2023**, *14*, 10181.

[10] M. Wang, S. Osella, R. Brescia, Z. Liu, J. Gallego, M. Cattelan, M. Crisci, S. Agnoli, T. Gatti, *Nanoscale* **2023**, *15*, 522.

[11] M. Wang, M. Crisci, M. Pavan, Z. Liu, J. Gallego, T. Gatti, *Catalysts* **2023**, *13*, 551.

[12] S. H. Choi, S. J. Yun, Y. S. Won, C. S. Oh, S. M. Kim, K. K. Kim, Y. H. Lee, *Nat. Commun.* **2022**, *13*, 1484.

[13] D. Rhodes, S. H. Chae, R. Ribeiro-Palau, J. Hone, *Nat. Mater.* **2019**, *18*, 541.

[14] F. Liu, *Prog. Surf. Sci.* **2021**, *96*, 100626.

[15] N. Curreli, M. Serri, D. Spirito, E. Lago, E. Petroni, B. Martín–García, A. Politano, B. Gürbulak, S. Duman, R. Krahne, V. Pellegrini, F. Bonaccorso, *Adv. Funct. Mater.* **2020**, *30*, 1908427.

[16] H. Chang, C. Tu, K. Lin, J. Pu, T. Takenobu, C. Hsiao, C. Chen, *Small* **2018**, *14*, 1802351.

[17] N. Curreli, M. Serri, M. I. Zappia, D. Spirito, G. Bianca, J. Buha, L. Najafi, Z. Sofer, R. Krahne, V. Pellegrini, F. Bonaccorso, *Adv. Electron. Mater.* **2021**, *7*, 2001080.

[18] A. J. Watson, W. Lu, M. H. D. Guimarães, M. Stöhr, *2D Mater.* **2021**, *8*, 032001.

[19] Z. Cai, B. Liu, X. Zou, H. M. Cheng, *Chem. Rev.* **2018**, *118*, 6091.

[20] F. Liu, W. Wu, Y. Bai, S. H. Chae, Q. Li, J. Wang, J. Hone, X.-Y. Zhu, *Science* **2020**, *367*, 903.

[21] M. Heyl, E. J. W. List-Kratochvil, *Appl. Phys. A* **2023**, *129*, 16.

[22] M. Velický, G. E. Donnelly, W. R. Hendren, W. J. I. DeBenedetti, M. A. Hines, K. S. Novoselov, H. D. Abruña, F. Huang, O. Frank, *Adv. Mater. Interfaces* **2020**, *7*, 2001324.

[23] A. C. Johnston, S. I. Khondaker, *Adv. Mater. Interfaces* **2022**, *9*, 2200106.

[24] Y. Huang, Y.-H. Pan, R. Yang, L.-H. Bao, L. Meng, H.-L. Luo, Y.-Q. Cai, G.-D. Liu, W.-J. Zhao, Z. Zhou, L.-M. Wu, Z.-L. Zhu, M. Huang, L.-W. Liu, L. Liu, P. Cheng, K.-H. Wu, S.-B. Tian, C.-Z. Gu, Y.-G. Shi, Y.-F. Guo, Z. G. Cheng, J.-P. Hu, L. Zhao, G.-H. Yang, E. Sutter, P. Sutter, Y.-L. Wang, W. Ji, X.-J. Zhou, et al., *Nat. Commun.* **2020**, *11*, 2453.

[25] M. Heyl, S. Grützmacher, S. Rühl, G. Ligorio, N. Koch, E. J. W. List–Kratochvil, *Adv. Mater. Interfaces* **2022**, *9*, 2200362.

[26] A. Grubišić-Čabo, M. Michiardi, C. E. Sanders, M. Bianchi, D. Curcio, D. Phuyal, M. H. Berntsen, Q. Guo, M. Dendzik, *Adv. Sci.* **2023**, *10*, 2301243.

[27] S. B. Desai, S. R. Madhvapathy, S. Amani, D. Kiriya, M. Hettick, M. Tosun, Y. Zhou, M. Dubey, J. W. Ager, D. Chrzan, A. Javey, *Adv. Mater.* **2016**, *28*, 4053.

[28] M. Velický, G. E. Donnelly, W. R. Hendren, S. McFarland, D. Scullion, W. J. I. DeBenedetti, G. C. Correa, Y. Han, A. J. Wain, M. A. Hines, D. A. Muller, K. S. Novoselov, H. D. Abruña, R. M. Bowman, E. J. G. Santos, F. Huang, *ACS Nano* **2018**, *12*, 10463.

[29] N. Petrini, A. Asaithambi, L. Rebecchi, N. Curreli, *Opt. Mater.: X* **2023**, *19*, 100255.

[30] A. Raja, L. Waldecker, J. Zipfel, Y. Cho, S. Brem, J. D. Ziegler, M. Kulig, T. Taniguchi, K. Watanabe, E. Malic, T. F. Heinz, T. C. Berkelbach, A. Chernikov, *Nat. Nanotechnol.* **2019**, *14*, 832.

[31] Y. Guo, X. Wei, J. Shu, B. Liu, J. Yin, C. Guan, Y. Han, S. Gao, Q. Chen, *Appl. Phys. Lett.* **2015**, *106*, 103109.

[32] D. Kufer, G. Konstantatos, *Nano Lett.* **2015**, *15*, 7307.

[33] M. Lafkioti, B. Krauss, T. Lohmann, U. Zschieschang, H. Klauk, K. V. Klitzing, J. H. Smet, *Nano Lett.* **2010**, *10*, 1149.

[34] M. Ben Haddada, J. Blanchard, S. Casale, J.-M. Krafft, A. Vallée, C. Méthivier, S. Boujday, *Gold Bull.* **2013**, *46*, 335.

[35] M. Sankar, Q. He, R. V. Engel, M. A. Sainna, A. J. Logsdail, A. Roldan, D. J. Willock, N. Agarwal, C. J. Kiely, G. J. Hutchings, *Chem. Rev.* **2020**, *120*, 3890.

[36] G. Feraco, O. D. Luca, A. Syari'ati, S. Hameed, A. A. El Yumin, J. Ye, R. G. Agostino, P. Rudolf, *J Phys. Mater.* **2023**, *6*, 034006.

[37] D.-h. Kang, S. R. Pae, J. Shim, G. Yoo, J. Jeon, J. W. Leem, J. S. Yu, S. Lee, B. Shin, J.-H. Park, *Adv. Mater.* **2016**, *28*, 7799.

[38] D. M. Sim, M. Kim, S. Yim, M.-J. Choi, J. Choi, S. Yoo, Y. S. Jung, *ACS Nano* **2015**, *9*, 12115.

[39] P. Topolovsek, F. Lamberti, T. Gatti, A. Cito, J. M. Ball, E. Menna, C. Gadermaier, A. Petrozza, *J. Mater. Chem. A* **2017**, *5*, 11882.

[40] E. Ji, K. Yang, J.-C. Shin, Y. Kim, J.-W. Park, J. Kim, G.-H. Lee, *Nanoscale* **2022**, *14*, 14106.

[41] S. Najmaei, X. Zou, D. Er, J. Li, Z. Jin, W. Gao, Q. Zhang, S. Park, L. Ge, S. Lei, J. Kono, V. B. Shenoy, B. I. Yakobson, A. George, P. M. Ajayan, J. Lou, *Nano Lett.* **2014**, *14*, 1354.

[42] A. Kröner, T. Hirsch, *Front. Chem.* **2020**, *7*, 927.

[43] L. Najafi, B. Taheri, B. Martín-García, S. Bellani, D. Di Girolamo, A. Agresti, R. Oropesa-Nuñez, S. Pescetelli, L. Vesce, E. Calabrò, M. Prato, A. E. Del Rio Castillo, A. Di Carlo, F. Bonaccorso, *ACS Nano* **2018**, *12*, 10736.

[44] C. A. Schneider, W. S. Rasband, K. W. Eliceiri, *Nat. Methods* **2012**, *9*, 671.

[45] S. Puebla, H. Li, H. Zhang, A. Castellanos-Gomez, *Adv. Photonics Res.* **2022**, *3*, 2100221.

[46] K. Kouroupis-Agalou, A. Liscio, E. Treossi, L. Ortolani, V. Morandi, N. M. Pugno, V. Palermo, *Nanoscale* **2014**, *6*, 5926.

[47] L. J. Ji, Y. Qin, D. Gui, W. Li, Y. Li, X. Li, P. Lu, *Chem. Mater.* **2018**, *30*, 8732.

[48] F. Montiel, N. Mokus, *Philos. Trans. R. Soc. A* **2022**, *380*, 20210257.

[49] A. C. Fowler, B. Scheu, *Proc. R. Soc. A: Math., Phys. Eng. Sci.* **2016**, *472*, 20150843.

[50] M. A. Gorokhovski, V. L. Saveliev, *Phys. Fluids* **2003**, *15*, 184.

[51] M. Magnozzi, T. Pflug, M. Ferrera, S. Pace, L. Ramó, M. Olbrich, P. Canepa, H. Ağircan, A. Horn, S. Forti, O. Cavalleri, C. Coletti, F. Bisio, M. Canepa, *J. Phys. Chem. C* **2021**, *125*, 16059.

[52] M. Ferrera, A. Sharma, I. Milekhin, Y. Pan, D. Convertino, S. Pace, G. Orlandini, E. Peci, L. Ramò, M. Magnozzi, C. Coletti, G. Salvan, D. R. T. Zahn, M. Canepa, F. Bisio, *J. Phys.: Condens. Matter* **2023**, *35*, 274001.

[53] E. Peci, M. Magnozzi, L. Ramó, M. Ferrera, D. Convertino, S. Pace, G. Orlandini, A. Sharma, I. Milekhin, G. Salvan, C. Coletti, D. R. T. Zahn, F. Bisio, M. Canepa, *Adv. Mater. Interfaces* **2023**, *10*, 2201586.

[54] J. D. Le Grange, J. L. Markham, C. R. Kurkjian, *Langmuir* **1993**, *9*, 1749.

[55] G. Kukucska, J. Koltai, *Phys. Status Solidi B* **2017**, *254*, 1700184.

[56] K. F. Mak, C. Lee, J. Hone, J. Shan, T. F. Heinz, *Phys. Rev. Lett.* **2010**, *105*, 136805.

[57] K. F. Mak, K. He, C. Lee, G. H. Lee, J. Hone, T. F. Heinz, J. Shan, *Nat. Mater.* **2013**, *12*, 207.

[58] J. S. Ross, S. Wu, H. Yu, N. J. Ghimire, A. M. Jones, G. Aivazian, J. Yan, D. G. Mandrus, D. Xiao, W. Yao, X. Xu, *Nat. Commun.* **2013**, *4*, 1474.

[59] S. Mouri, Y. Miyauchi, K. Matsuda, *Nano Lett.* **2013**, *13*, 5944.

[60] M. Buscema, G. A. Steele, H. S. J. van der Zant, A. Castellanos-Gomez, *Nano Res.* **2014**, *7*, 561.

[61] C. Lee, H. Yan, L. E. Brus, T. F. Heinz, J. Hone, S. Ryu, *ACS Nano* **2010**, *4*, 2695.

[62] C. Rice, R. J. Young, R. Zan, U. Bangert, D. Wolverson, T. Georgiou, R. Jalil, K. S. Novoselov, *Phys. Rev. B* **2013**, *87*, 081307.

[63] H. Li, Q. Zhang, C. C. R. Yap, B. K. Tay, T. H. T. Edwin, A. Olivier, D. Baillargeat, *Adv. Funct. Mater.* **2012**, *22*, 1385.

[64] B. Chakraborty, A. Bera, D. V. S. Muthu, S. Bhowmick, U. V. Waghmare, A. K. Sood, *Phys. Rev. B* **2012**, *85*, 161403.

[65] M. Ghini, E. S. Yanev, C. Kastl, K. Zhang, A. W. Jansons, B. M. Crockett, K. M. Koskela, E. S. Barnard, E. Penzo, J. E. Hutchison, J. A. Robinson, L. Manna, N. J. Borys, P. J. Schuck, I. Kriegel, *Adv. Photonics Res.* **2021**, *2*, 2000151.

[66] V. P. Pham, G. Y. Yeom, *Adv. Mater.* **2016**, *28*, 9024.

[67] M. Velický, A. Rodriguez, M. Bouša, A. V. Krayev, M. Vondráček, J. Honolka, M. Ahmadi, G. E. Donnelly, F. Huang, H. D. Abruña, K. S. Novoselov, O. Frank, *J. Phys. Chem. Lett.* **2020**, *11*, 6112.

[68] S. Golovynskyi, O. I. Datsenko, D. Dong, Y. Lin, I. Irfan, B. Li, D. Lin, J. Qu, *J. Phys. Chem. C* **2021**, *125*, 17806.

[69] S. Park, N. Mutz, T. Schultz, S. Blumstengel, A. Han, A. Aljarb, L.-J. Li, E. J. W. List-Kratochvil, P. Amsalem, N. Koch, *2D Mater.* **2018**, *5*, 025003.

[70] K. M. McCreary, A. T. Hanbicki, S. V. Sivaram, B. T. Jonker, *APL Mater.* **2018**, *6*, 111106.

[71] Y. Liu, T. Shen, S. Linghu, R. Zhu, F. Gu, *Nano Adv.* **2022**, *4*, 2484.

[72] D. Ganta, S. Sinha, R. T. Haasch, *Surf. Sci. Spectra* **2014**, *21*, 19.

[73] Y.-Y. Song, H. Hildebrand, P. Schmuki, *Surf. Sci.* **2010**, *604*, 346.

[74] N. Graf, E. Yegen, T. Gross, A. Lippitz, W. Weigel, S. Krakert, A. Terfort, W. E. S. Unger, *Surf. Sci.* **2009**, *603*, 2849.

[75] Y. Huang, E. Sutter, N. N. Shi, J. Zheng, T. Yang, D. Englund, H.-J. Gao, P. Sutter, *ACS Nano* **2015**, *9*, 10612.

[76] Q. Le, M. Claes, T. Conard, E. Kesters, M. Lux, G. Vereecke, *MicroElectron. Eng.* **2009**, *86*, 181.

[77] M. Sypabekova, A. Hagemann, D. Rho, S. Kim, *Biosensors* **2022**, *13*, 36.

[78] Y. Li, Y. Kong, J. Peng, C. Yu, Z. Li, P. Li, Y. Liu, C.-F. Gao, R. Wu, *J. Materiomics* **2019**, *5*, 413.

[79] J.-P. Wu, L. Wang, L.-Y. Zhang, *Rare Met.* **2017**, *36*, 698.

[80] Y. Lee, S. Chang, S. Chen, S. Chen, H. Chen, *Adv. Sci.* **2022**, *9*, 2102128.